

# Research on a Neutron Detector with a Boron-Lined Multilayer Converter

Chao Deng, Qin Hu, Pengcheng Li, Qibiao Wang , Bo Xie , Jianbo Yang and Xianguo Tuo \*

School of Physics and Electronic Engineering, Sichan University of Science and Engineering, Zigong 643000, China; ray\_9eng@163.com (C.D.); hq\_suse@163.com (Q.H.); lpc\_cdut@163.com (P.L.); xiebo@suse.edu.cn (B.X.); yjb@suse.edu.cn (J.Y.)

\* Correspondence: tuoxg@cdut.edu.cn

**Abstract:**  $^3\text{He}$  is a splendid neutron detection material due to its high neutron reaction cross section, gaseous state, and nonelectronegative and nonpoisonous nature. With the worldwide problem of the “ $^3\text{He}$  supply crisis” arising, boron-lined gaseous neutron detectors are being widely used in neutron detection to replace  $^3\text{He}$  neutron detectors. In this work, to reduce the scattering neutron background coming from the substrate of a boron-lined neutron detector in the application of neutron scattering, a new design of the boron-lined gaseous neutron detector composed of a boron-lined multichip converter and a multiwire proportional chamber was proposed. The electron drift efficiency matrix simulated by Garfield++ (Version 2023.4) and the values and positions of electron energy deposition simulated by Geant4 were obtained. The  $\alpha$ ,  $^7\text{Li}$ , and total charged particle energy deposition spectra were acquired via coupling calculations of the electron drift efficiency matrix and the values and positions of electron energy deposition, and the width of the slit was selected as 3 mm. The boron-lined multilayer converter neutron detector (BMCND) was tested using a  $^{241}\text{Am}$ – $^{239}\text{Pu}$  mixture  $\alpha$  source, and the total count rate of  $\alpha$  charged particles was measured as  $599.5\text{ s}^{-1}$ , which is 89% of the theoretical  $\alpha$  particle emission rate of  $672.9\text{ s}^{-1}$ . The drift voltage experiments showed that 1200 V is enough to acquire a relatively ideal count, and a 2500 V drift voltage was confirmed, considering the higher count and instrument safety. We also performed the neutron detection experiments using a photo-neutron source, and a characteristic spectrum shape of “two stairs” was measured. When borated polyethylene was used to shield the BMCND, the detected total count decreased while keeping the characteristic spectrum shape, demonstrating that the BMCND was equipped with the ability to detect neutrons, indicating that BMCNDs have the potential to be an outstanding  $^3\text{He}$  alternative neutron detector.

**Keywords:** boron-lined neutron detector; BMCND; electron drift efficiency; energy deposition spectrum; neutron detection efficiency



**Citation:** Deng, C.; Hu, Q.; Li, P.; Wang, Q.; Xie, B.; Yang, J.; Tuo, X. Research on a Neutron Detector with a Boron-Lined Multilayer Converter. *Appl. Sci.* **2024**, *14*, 4269. <https://doi.org/10.3390/app14104269>

Academic Editor: Richard Kouzes

Received: 24 April 2024

Revised: 11 May 2024

Accepted: 14 May 2024

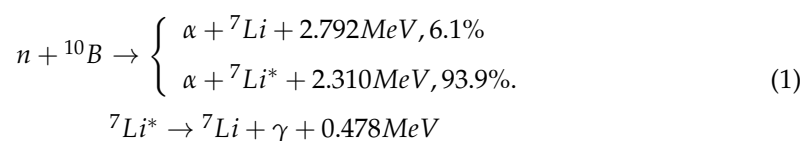
Published: 17 May 2024



**Copyright:** © 2024 by the authors. Licensee MDPI, Basel, Switzerland. This article is an open access article distributed under the terms and conditions of the Creative Commons Attribution (CC BY) license (<https://creativecommons.org/licenses/by/4.0/>).

## 1. Introduction

The boron-lined gaseous detector, which is an excellent  $^3\text{He}$  alternative neutron detector [1,2], is studied by many researchers to address the “ $^3\text{He}$  supply crisis” worldwide problem [3–5]. This detector is widely applied in various fields, such as homeland security [6,7], cosmic ray neutron sensing [8,9], and large neutron spectrometers [10–14]. As a result, various boron-lined gaseous detectors with different structures have been proposed, such as boron-coated straw detectors [15,16], multigridded detectors [17,18], boron-lined honeycomb detectors [19–21], multibladed detectors [22,23], and GEM-based detectors [24–27]. All these detectors have the same neutron detection principle, which relies on the  $^{10}\text{B}$  isotope capture neutron nuclear reaction  $^{10}\text{B}(n, \alpha)^7\text{Li}$ , which can convert neutrons into charged particles. The abundance of  $^{10}\text{B}$  nuclides is 19.8%, and the cross section of  $^{10}\text{B}$  atoms to thermal neutrons is approximately 3844 barns. The capture reaction equation is as follows:



During the process of thermal neutron detection,  $\alpha$  and  ${}^7\text{Li}$  charged particles are produced in the boron film as the incident neutrons are being absorbed by the  ${}^{10}\text{B}$  atoms, distributing the reaction energy (2.792 and 2.310 MeV with branching ratios of 6.1% and 93.9%, respectively) according to the conservation of energy and momentum. In addition, the  $\alpha$  and  ${}^7\text{Li}$  particles move in a backward direction because the thermal neutron kinetic energy (25.3 meV) is far smaller than the reaction energy. Therefore, only one particle has the possibility of penetrating the boron film and entering the working gas, which could produce electrons after being ionized by charged particles. Then, a nuclear signal is produced when these electrons are multiplied and collected by the anode. Based on the aforementioned neutron detection principle, in order to achieve a higher neutron detection efficiency, the incident neutrons should penetrate the multilayer boron film, which is attached to the aluminum substrate. In this way, the incident neutrons cannot help but penetrate the multilayer substrate, leading to an increase in the number of scattered neutrons and deteriorating the signal-to-background ratio [28]. Therefore, a new detector structure has been proposed to detect the incident neutrons directly, avoiding the neutrons penetrating multilayer substrates. This structure comprises a boron-lined honeycomb neutron converter and an electron multiplier named the boron-lined honeycomb neutron detector [20,21]. However, the boron-lined honeycomb neutron converter's substrate is aramid paper, making it challenging to ensure that the structural parameters of each honeycomb hole are equal. This issue can lead to a deterioration in the value and uniformity of the neutron detection efficiency. This study proposes a new design for the boron-lined gaseous neutron detector, called the boron-lined multilayer converter neutron detector (BMCND), to solve the above problem. The BMCND's structure parameters were optimized using Geant4 [29–31] and Garfield++(Version 2023.4) [32,33]. Based on the optimized parameters, the BMCND was constructed in conjunction with our previous boron-lined method study [34,35]. To test the BMCND, we used a  ${}^{241}\text{Am}$ – ${}^{239}\text{Pu}$  mixture  $\alpha$  source and a photo-neutron source. The results show that the BMCND is equipped with the capability to detect neutrons, indicating that the BMCND has the potential to be an outstanding  ${}^3\text{He}$ -alternative neutron detector.

## 2. Physical Design and Optimization

The BMCND's physical structure consists of a boron-lined multichip converter (BMC) and a multiwire proportional chamber (MWPC) [36,37], which are secured by eight fasteners, as shown in Figure 1. The BMC, with a size of  $100 \times 100 \times 100 \text{ mm}^3$  and composed of 34 pieces of boron-lined ultrathin glass with a 3 mm slit, is placed between the rectangular cathode and protection ring with voltages of  $-2500 \text{ V}$  and  $0 \text{ V}$ , respectively. The upper section of the protection ring is the MWPC with voltages of  $25$ – $1160 \text{ V}$ , and the MWPC could act as a position-sensitive detector through adding specific electronic readouts. The boron-lined ultrathin glass includes one piece of ultrathin glass with a thickness of  $150 \mu\text{m}$  and two pieces of a natural boron layer with a thickness of  $20 \mu\text{m}$ , which are attached to both sides of the ultrathin glass using epoxy resin [34]. A field cage surrounds the boron-lined multilayer converter to provide a uniform drift electric field. This cage comprises flexible printed circuits comprising 47 pieces of a thin copper sheet connected by the same resistance value. The MWPC consists of two sets of orthogonal gold-plated tungsten wires secured by the rectangular printed circuit board, forming cathode and anode reels. The cathode and anode reels include 64 and 32 gold-plated tungsten wires with diameters of  $60 \mu\text{m}$  and  $20 \mu\text{m}$ , respectively. All these components are sealed in an aluminum chamber with a thickness of 3 mm and filled with working gas ( $\text{Ar}:\text{CO}_2 = 90:10$ ).

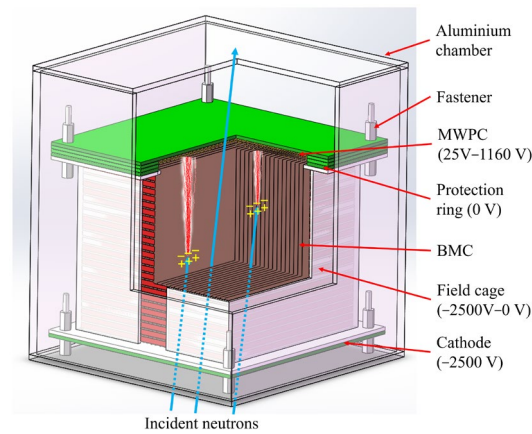


**Figure 1.** Physical structure of the BMCND.

Figure 2 shows the schematic diagram of the BMCND's neutron detection process. The incident neutrons enter the BMCND at an angle of about  $1.72^\circ$ , which is the most excellent angle for neutron detection efficiency based on the size of the BMC, with its 100 mm length and 3 mm slit [38]. As a result, all the boron films can react with the incident neutrons, thereby increasing the neutron detection efficiency. The incident neutrons are absorbed by the boron film through the nuclear reaction  $^{10}\text{B}(n, \alpha)^7\text{Li}$ , and  $\alpha$  and  $^7\text{Li}$  charged particles are produced. One of these charged particles has the possibility of penetrating the boron film, entering the working gas, and ionizing and producing electrons. The electric field provided by the field cage carries these electrons to the MWPC, where a nuclear signal is generated when the electrons undergo multiplication and are collected.

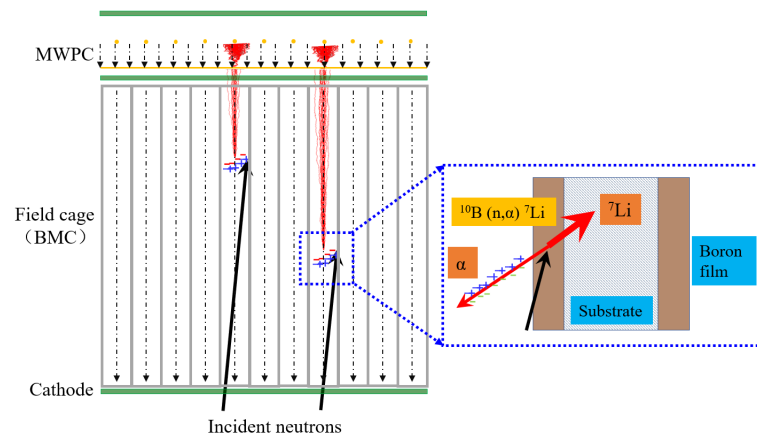


**Figure 2.** Neutron detection schematic diagram of the BMCND.

This study optimizes the width of the slit (WOS) for better neutron detection since it affects the electron drift efficiency (EDE) and the surface area of the boron film, both of which have an impact on neutron detection. The electron drift efficiency matrix (EDEM) was established to calculate the neutron detection efficiency at all points of the slit. One of the slit models was established, as shown in Figure 3, after considering that all the slits have the same geometric parameters. At the same time, the Y and Z axes were along the slit direction, with a total length of 10 cm. However, the X axis was in the vertical slit direction, i.e., along the WOS. The chosen WOS values were 2.0 mm, 2.5 mm, 3.0 mm, 3.5 mm, and 4.0 mm, based on experience. The Y and Z axes were discretized with a 0.5 cm space between them, while the X axis was discretized with a space of 0.1 mm, forming a three-dimensional lattice of the slit. The EDE at every point in the three-dimensional lattice was simulated one by one with Garfield++, with an initial electron kinetic energy of 0.01 eV and  $10^5$  electrons, to obtain the EDEM at the different WOS values.

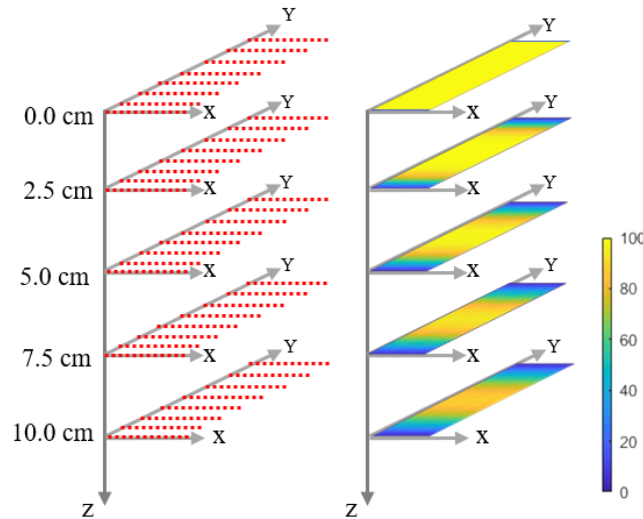


Figure 3. Schematic diagram of electrons' initial positions.

Figure 4 shows an example of an EDEM with a 3 mm slit. All the EDEMs with different widths of slits have the same transformation law. The EDE decreases gradually as the drift distance increases from  $z = 0$  to 10.0 cm. When the drift distance,  $z$ , is fixed, the EDE is more extensive and closer to the center. The process of neutron detection for the different slits was simulated using Geant4 to acquire the values and positions of electron energy deposition. The Geant4 simulation parameters are as follows: (a) the thermal neutron energy is 25.3 meV; (b) the physics list is QGSP\_BERT\_HP; (c) the cross-section database is G4NDL4.5; and (d) the number of incident neutrons is  $10^7$ . We calculated the charged particle energy deposition spectrum (EDS) of different slits by coupling the EDEM with the values and positions of electron energy deposition, as shown in Figure 5.

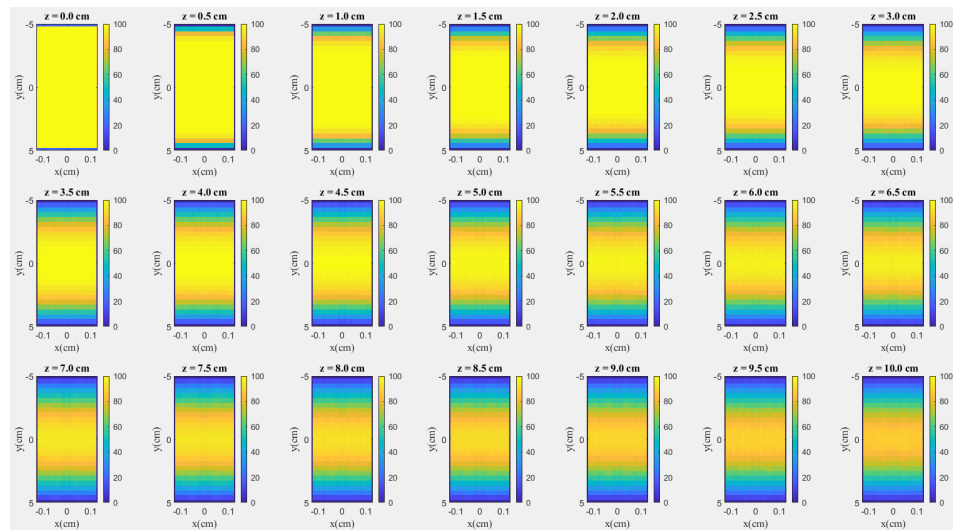
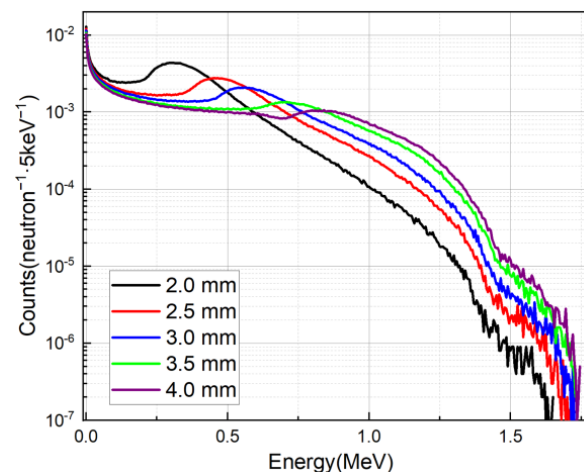


Figure 4. EDEM with a 3 mm slit.

The simulation results showed that the neutron detection efficiencies were 34.39%, 30.16%, 28.04%, 25.42%, and 24.04% for a WOS of 2.0 mm, 2.5 mm, 3.0 mm, 3.5 mm, and 4.0 mm, respectively. Figure 5 shows that all the EDSs of the different slits display the shape of “two stairs”. The edge of the “two stairs” moves to the right as the value of the WOS increases. A higher value of the WOS is required since electronic noise may saturate the low-energy section of the charged particle energy deposition spectrum. The value of the WOS was set to 3.0 mm, considering noise effects and neutron detection efficiency.



**Figure 5.** Charged particle EDS of different slits.

Figure 6 displays the analysis of the  $\alpha$ ,  ${}^7\text{Li}$ , and total charged particle EDS compositions. As observed, the first stair consists of  $\alpha$  and  ${}^7\text{Li}$  together, and the second stair consists of  ${}^7\text{Li}$ . We stimulated the EDS of gamma rays with energies of 662 keV from  ${}^{137}\text{Cs}$  and 478 keV produced by  ${}^7\text{Li}^*$ . The energy threshold was calculated as 46.1 keV to determine that the neutron signals could reject 99% of the gamma signals. Hence, the gamma rays hardly affected the neutron detection efficiency of the BMCND.

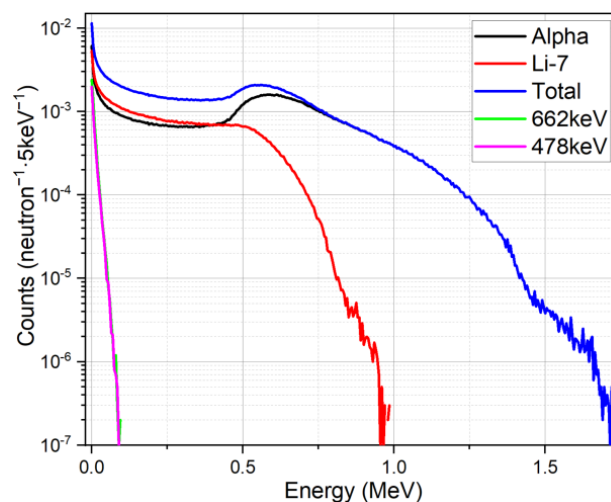


**Figure 6.** EDS of different particles.

### 3. Experiments with ${}^{241}\text{Am}$ – ${}^{239}\text{Pu}$ Mixture Source

Figure 7 depicts the BMCND packaging process. A resin bracket, manufactured by 3D printing technology, supports the field cage and boron-lined ultrathin glass. One by one, the boron-lined ultrathin glass was inserted into each resin bracket card slot and secured with hot melt adhesive after the field cage had been fastened within the resin bracket using polyimide tape. A manufactured BMC and an MWPC were connected by eight plastic screws and nuts, sealed into the aluminum chamber, to complete the BMCND packaging.

We applied a  ${}^{241}\text{Am}$ – ${}^{239}\text{Pu}$  mixture  $\alpha$  source to verify the ability of the BMCND to detect charged particles. Figure 8 displays the schematic diagram of the  $\alpha$  radioactive source experiment. The  ${}^{241}\text{Am}$ – ${}^{239}\text{Pu}$  mixture  $\alpha$  source was fixed on the cathode before the boron-lined ultrathin glass was installed. One ORTEC 556 high-voltage power supply (Atlanta, GA, USA) was used to provide  $-2500$  V to the cathode, and another was used to provide  $+1160$  V to the CAEN 1422 preamplifier (Viareggio, Italy), which provided a bias voltage to the anode reel of the MWPC. A ground electrode was used to provide  $0$  V

to the protection ring. Meanwhile, the nuclear signals were led into an oscilloscope from the CAEN 1422 preamplifier and ORTEC 672 main amplifier (Atlanta, GA, USA). Nuclear Instrumentation Module bins provided the power supply for the ORTEC 556 and ORTEC 672. Finally, the computer stored the nuclear signal from the ORTEC 672 main amplifier after dealing with the ORTEC EASY-MCA (Atlanta, GA, USA).

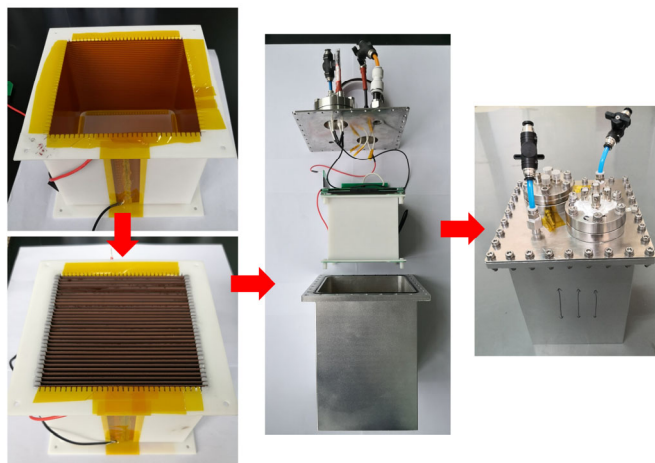


Figure 7. BMCND packaging process.

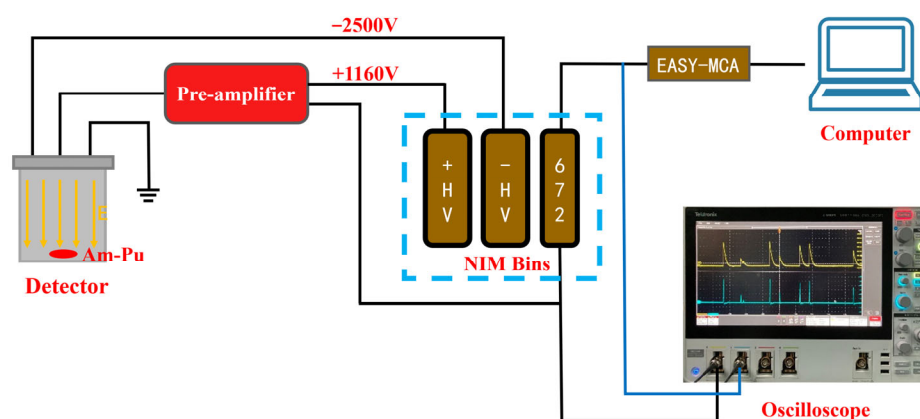


Figure 8. Schematic diagram of  $\alpha$  radioactive source experiment.

A radioactive source, AMPU1103, employed by the  $^{241}\text{Am}$ – $^{239}\text{Pu}$  mixture  $\alpha$  source, was provided by the CAEA Innovation Center of Nuclear Environmental Safety Technology of Southwest University of Science and Technology. Table 1 shows the detailed information. The mixture source mainly comprises  $^{241}\text{Am}$  and  $^{239}\text{Pu}$  nuclides with  $2\pi$   $\alpha$  charged particle emission rates of  $282.2\text{ s}^{-1}$  and  $390.7\text{ s}^{-1}$ , respectively, where the total emission rate is  $672.9\text{ s}^{-1}$ . The reference time is 10 August 2011, and the expanded uncertainty ( $k = 2$ ) is 2.5%. The  $\alpha$  charged particle characteristic kinetic energy of  $^{241}\text{Am}$  and  $^{239}\text{Pu}$  is 5.486 MeV and 5.157 MeV, respectively, referring to the nuclide database.

Table 1. Detailed information about the  $\alpha$  radioactive source used.

Source Number	Nuclide	Particle Emission Rate over $2\pi$ ( $\text{s}^{-1}$ )
AMPU1103	Am-241	282.2
	Pu-239	390.7
Reference Time	10 August 2011	
Expanded Uncertainty ( $k = 2$ )	2.5%	

Figure 9 depicts the layout of the  $\alpha$  radioactive source experiment, as shown in Figure 8. The results of  $\alpha$  radioactive source experiments are shown in Figure 10, indicating that no nuclear signal was seen other than noise when there was no  $^{241}\text{Am}$ - $^{239}\text{Pu}$   $\alpha$  source. On the contrary, we observed many nuclear signals when the  $^{241}\text{Am}$ - $^{239}\text{Pu}$   $\alpha$  source was used. The two recorded Gaussian peaks, for the  $^{241}\text{Am}$  nuclide at 5.486 MeV and for the  $^{239}\text{Pu}$  nuclide at 5.157 MeV, correspond to two kinds of  $\alpha$  charged particles. Moreover, low-energy  $\alpha$  particles have higher counts, and high-energy  $\alpha$  particles have lower counts, agreeing with the original provided data on  $\alpha$  particles. The calculated total measured count rate is  $599.5\text{ s}^{-1}$ , 89% of the theoretical  $\alpha$  particle emission rate of  $672.9\text{ s}^{-1}$ .

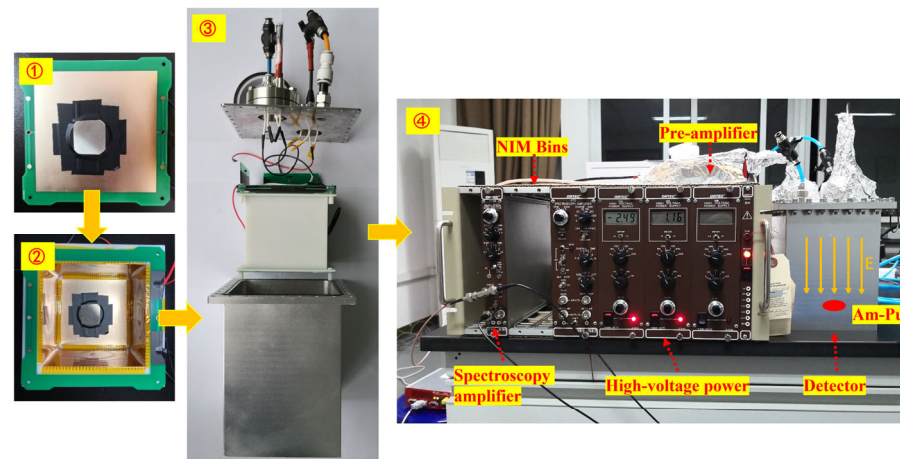


Figure 9. Layout of  $\alpha$  radioactive source experiment.

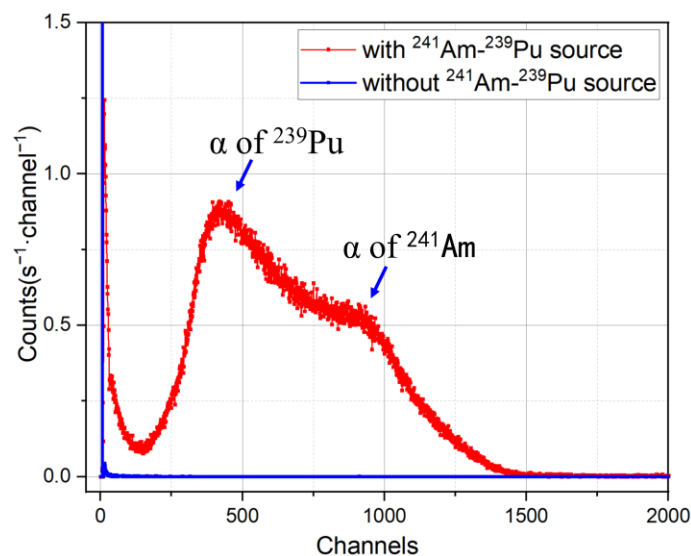


Figure 10. Results of  $\alpha$  radioactive source experiment.

Total counts with different drift voltages were measured, as shown in Figure 11, indicating that the drift voltage increases with a rise in total counts. When the drift voltage is less than 1200 V, the increasing slope is bigger when it is greater than 1200 V. In other words, the total counts reach a relatively high level when the drift voltage is up to 1200 V. As a result, a higher drift voltage is needed when higher total counts are desired. Thus, the drift voltage was confirmed to be 2500 V, in light of the safety of an ORTEC 556 high-voltage power supply, with a maximum supplied voltage of 3000 V.

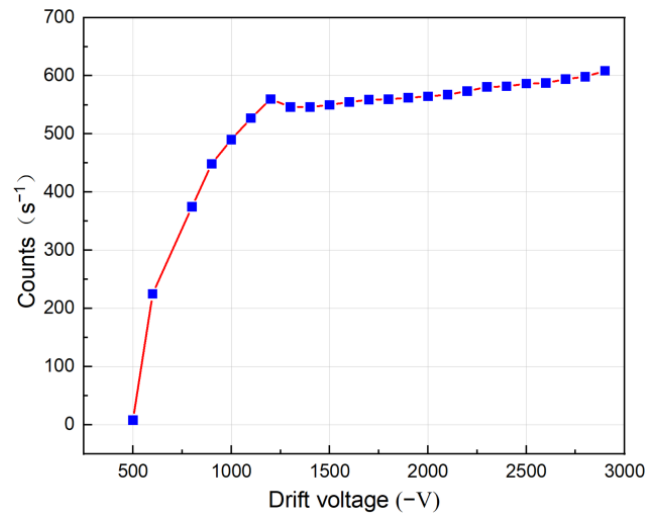


Figure 11. Results of different drift voltage experiments.

#### 4. Experiments with Photo-Neutron Source

The capacity of the BMCND to detect neutrons was tested using a photo-neutron source [39]. Figure 12 shows the layout of the photo-neutron source experiment based on the schematic diagram of the  $\alpha$  radioactive source experiment shown in Figure 8. The neutron spectrum is referred to in Ref. [40].

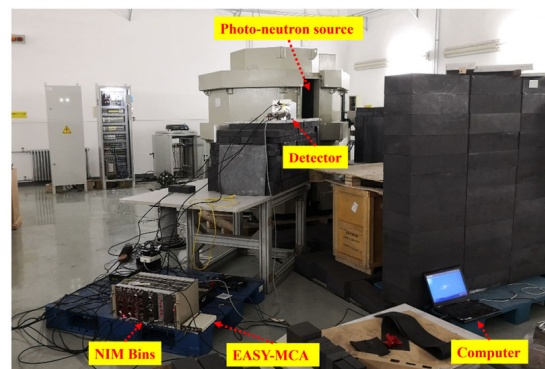


Figure 12. Layout of photo-neutron source experiment.

Figure 13 presents the test results of the photo-neutron source experiments, which included three kinds of measuring conditions: “Accelerator on+ without shielding”, “Accelerator on+ with shielding” and “Accelerator off+ without shielding”. The BMCND is encased in a 5 cm thick layer of borated polyethylene with a mass fraction of 5% as the shielding condition. Except for noise, there is hardly any nuclear signal when the accelerator is off. When the accelerator is on, the spectrum shape of “two stairs” implies that the first one is contributed to by  $\alpha$  and  ${}^7\text{Li}$  particles. The second one is derived from  $\alpha$  particles only and is present whether there is shielding or not. When the borated polyethylene surrounds the BMCND, the total counts decrease, but the spectrum shape of “two stairs” is maintained, indicating that neutrons are detected.

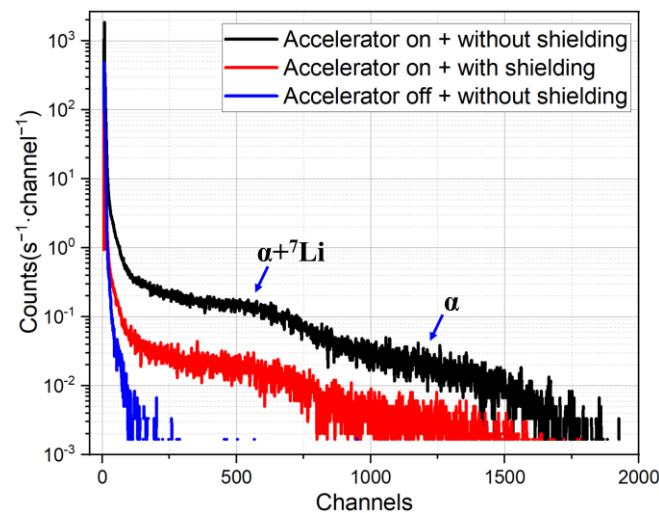


Figure 13. Results of photo-neutron source experiments.

## 5. Conclusions

This study proposes a new design for a boron-lined gaseous neutron detector structure comprising a BMC and an MWPC to address the “ $^3\text{He}$  supply crisis” global problem while avoiding a scattering neutron background coming from the substrate of the boron-lined neutron detector. We established EDEMs with different slit widths using Garfield++ because the process of electron drifting occurs in BMCND neutron detection. The Geant4 simulation obtained the values and positions of electron energy deposition. We calculated the charged particle energy deposition spectra of different slits with widths of 2.0 mm, 2.5 mm, 3.0 mm, 3.5 mm, and 4.0 mm by coupling the EDEMs and the values and positions of electron energy deposition. The width of the slit was selected as 3 mm, considering comprehensively noise effects and neutron detection efficiency. The measured  $\alpha$  particle count rate was  $599.5 \text{ s}^{-1}$ , 89% of the theoretical emission rate of  $672.9 \text{ s}^{-1}$ . Moreover, a  $^{241}\text{Am}$ – $^{239}\text{Pu}$  mixture  $\alpha$  radioactive source was used to test the BMCND, indicating that the BMCND has the capacity for  $\alpha$  charged particle detection. The results of the drift voltage experiments demonstrate that 1200 V can acquire a relatively ideal count, confirming a 2500 V drift voltage, considering higher counts and instrument safety. The results of the photo-neutron source experiments show that the characteristic spectrum shape of “two stairs” was measured. When the borated polyethylene was used to shield the BMCND, the detected total count decreased while keeping the characteristic spectrum shape, which demonstrates that the BMCND is equipped with the ability to detect neutrons, indicating that the BMCND could be an outstanding  $^3\text{He}$ -alternative neutron detector. A future study will present more experimental results with neutron detection efficiency calibrations.

**Author Contributions:** Conceptualization, C.D. and Q.W.; data curation, Q.H. and B.X.; methodology, C.D. and Q.H.; writing—original draft preparation, C.D. and B.X.; writing—review and editing, P.L. and J.Y.; project administration, J.Y. and X.T.; funding acquisition, X.T. and Q.W. All authors contributed to discussing and analyzing the results. All authors have read and agreed to the published version of the manuscript.

**Funding:** We are grateful for the support received from the National Natural Science Foundation of China (Grant No. 42004151), the National Defense Technology Foundation Program of China (Grant No. JSJT2022209A001-3), the Sichuan Science and Technology Program (Grant No. 2023NSFSC1315), the Talent Project of Sichuan University of Science and Engineering (Grant No. 2021RC14), and the Scientific Research and Innovation Team Program of Sichuan University of Science and Engineering (Grant No. SUSE652A001).

**Institutional Review Board Statement:** Not applicable.

**Informed Consent Statement:** Not applicable.

**Data Availability Statement:** All the data generated and analyzed during this study are included in this paper or are available from the corresponding authors upon reasonable request.

**Acknowledgments:** We thank Yang Yigang of Tsinghua University for providing the neutron beams from the photo-neutron source. We thank the CAEA Innovation Center of Nuclear Environmental Safety Technology of Southwest University of Science and Technology for providing the  $^{241}\text{Am}$ – $^{239}\text{Pu}$  mixture  $\alpha$  radioactive source.

**Conflicts of Interest:** The authors declare no conflicts of interest.

## References

1. Hurd, A.J.; Kouzes, R.T. Why new neutron detector materials must replace helium-3. *Eur. Phys. J. Plus* **2014**, *129*, 1–3. [[CrossRef](#)]
2. Kouzes, R.T.; Lintereur, A.T.; Siciliano, E.R. Progress in alternative neutron detection to address the helium-3 shortage. *Nucl. Instrum. Methods Phys. Res. Sect. A Accel. Spectrometers Detect. Assoc. Equip.* **2015**, *784*, 172–175. [[CrossRef](#)]
3. Kouzes, R.T. *The  $^3\text{He}$  Supply Problem*; Pacific Northwest National Lab. (PNNL): Richland, WA, USA, 2009.
4. Shea, D.A.; Morgan, D.L. *The Helium-3 Shortage: Supply, Demand, and Options for Congress*; Congressional Research Service: Washington, DC, USA, 2010.
5. Arkharov, A.M.; Arkharov, I.A.; Dolgopyatov, D.A.; Bondarenko, V.L.  $^3\text{He}$  supply crisis: Reasons and challenges. *Chem. Petrol. Eng.* **2013**, *49*, 41–45. [[CrossRef](#)]
6. Lacy, J.L.; Athanasiades, A.; Martin, C.S.; Sun, L.; Vazquez-Flores, G.J.; Lyons, T.D. Boron-coated straw detectors: A novel approach for helium-3 neutron detector replacement. In Proceedings of the IEEE Nuclear Science Symposium & Medical Imaging Conference, Knoxville, TN, USA, 30 October–6 November 2010; pp. 3971–3975.
7. Lacy, J.L.; Athanasiades, A.; Martin, C.S.; Sun, L.; Vazquez-Flores, G.J. Boron-coated straw detectors for backpack monitors. *IEEE Trans. Nucl. Sci.* **2013**, *60*, 1111–1117. [[CrossRef](#)]
8. Weimar, J.; Köhli, M.; Allmendinger, F.; Schmidt, U. Large-scale boron-lined neutron detectors for Cosmic-Ray Neutron Sensing. *Geophys. Res. Abstr.* **2019**, *21*, 1.
9. Weimar, J.; Köhli, M.; Budach, C.; Schmidt, U. Large-scale boron-lined neutron detection systems as a  $^3\text{He}$  alternative for cosmic ray neutron sensing. *Front. Water* **2020**, *2*, 544806. [[CrossRef](#)]
10. Deng, C.; Tuo, X.; Peng, S.; Yu, Y.; Fang, Z.; Wang, Q.; Liu, L.; Yang, Y. An angular sensitivity study of the boron-lined honeycomb convertor neutron detector used for the small angle neutron scattering. In Proceedings of the 2019 IEEE Nuclear Science Symposium and Medical Imaging Conference (NSS/MIC), Manchester, UK, 26 October–2 November 2019; pp. 1–3.
11. Piscitelli, F.; Mauri, G.; Messi, F.; Anastasopoulos, M.; Arnold, T.; Glavic, A.; Höglund, C.; Ilves, T.; Higuera, I.L.; Pazmandi, P.; et al. Characterization of the Multi-Blade 10B-based detector at the CRISP reflectometer at ISIS for neutron reflectometry at ESS. *J. Instrum.* **2018**, *13*, P05009. [[CrossRef](#)]
12. Anastasopoulos, M.; Bebb, R.; Berry, K.; Birch, J.; Brys, T.; Buffet, J.-C.; Clergeau, J.-F.; Deen, P.; Ehlers, G.; Van Esch, P.; et al. Multi-Grid detector for neutron spectroscopy: Results obtained on time-of-flight spectrometer CNCS. *J. Instrum.* **2017**, *12*, P04030. [[CrossRef](#)]
13. Piscitelli, F. Novel boron-10-based detectors for neutron scattering science: Helium-3-free detectors for large-and small-area applications: The Multi-Grid and the Multi-Blade prototypes. *Eur. Phys. J. Plus* **2015**, *130*, 1–9. [[CrossRef](#)]
14. Albani, G.; Cippo, E.P.; Croci, G.; Muraro, A.; Schooneveld, E.; Scherillo, A.; Hall-Wilton, R.; Kanaki, K.; Höglund, C.; Hultman, L.; et al. Evolution in boron-based GEM detectors for diffraction measurements: From planar to 3D converters. *Meas. Sci. Technol.* **2016**, *27*, 115902. [[CrossRef](#)]
15. Lacy, J.L.; Athanasiades, A.; Sun, L.; Martin, C.S.; Lyons, T.D.; Foss, M.A.; Haygood, H.B. Boron-coated straws as a replacement for  $^3\text{He}$ -based neutron detectors. *Nucl. Instrum. Methods Phys. Res. Sect. A Accel. Spectrometers Detect. Assoc. Equip.* **2011**, *652*, 359–363. [[CrossRef](#)]
16. Chen, C.; Gong, H.; Yang, Y.; Zhu, S.; Huang, T.; Wang, Y.; Wang, X.; Li, Y. Realization and test of position sensitive boron coated straw-tube. In Proceedings of the 2013 IEEE Nuclear Science Symposium and Medical Imaging Conference (2013 NSS/MIC), Seoul, Republic of Korea, 27 October–2 November 2013; pp. 1–4.
17. Birch, J.; Buffet, J.C.; Correa, J.; van Esch, P.; Guérard, B.; Hall-Wilton, R.; Höglund, C.; Hultman, L.; Khaplanov, A.; Piscitelli, F.  $^{10}\text{B}_4\text{C}$  Multi-Grid as an Alternative to  $^3\text{He}$  for Large Area Neutron Detectors. *IEEE Trans. Nucl. Sci.* **2013**, *60*, 871–878. [[CrossRef](#)]
18. Khaplanov, A. Multi-Grid Boron-10 detector for large area applications in neutron scattering science. *arXiv* **2012**, arXiv:1209.0566.
19. Yang, Y.; Li, C.; Chen, C.; Wang, X.; Li, Y. Research of boron lined honey-neutron detector realized with atomic layer deposition. In Proceedings of the 2013 IEEE Nuclear Science Symposium and Medical Imaging Conference (2013 NSS/MIC), Seoul, Republic of Korea, 26 October–2 November 2013; pp. 1–3.
20. Fang, Z.; Yang, Y.; Li, Y. The research of high detection efficiency boron lined detector with a honeycomb neutron converter. In Proceedings of the 2015 IEEE Nuclear Science Symposium and Medical Imaging Conference (NSS/MIC), San Diego, CA, USA, 31 October–7 November 2015; pp. 1–4.
21. Fang, Z.; Yang, Y.; Li, Y.; Zhang, Z.; Wang, X. Research on a neutron detector with a boron-lined honeycomb neutron converter. *IEEE Trans. Nucl. Sci.* **2017**, *64*, 1048–1055. [[CrossRef](#)]

22. Mauri, G.; Apostolidis, I.; Christensen, M.J.; Glavic, A.; Lai, C.C.; Laloni, A.; Messi, F.; Olsson, A.L.; Robinson, L.; Stahn, J.; et al. The Multi-Blade Boron-10-based neutron detector performance using a focusing reflectometer. *J. Instrum.* **2020**, *15*, P03010. [[CrossRef](#)]
23. Piscitelli, F.; Messi, F.; Anastasopoulos, M.; Bryś, T.; Chicken, F.; Dian, E.; Fuzi, J.; Höglund, C.; Kiss, G.; Orban, J.; et al. The Multi-Blade Boron-10-based neutron detector for high intensity neutron reflectometry at ESS. *J. Instrum.* **2017**, *12*, P03013. [[CrossRef](#)]
24. Yang, L.; Zhou, J.R.; Sun, Z.J.; Zhang, Y.; Huang, C.-Q.; Sun, G.-A.; Wang, Y.-F.; Yang, G.-A.; Xu, H.; Xie, Y.-G.; et al. Experimental research on a THGEM-based thermal neutron detector. *Chin. Phys. C* **2015**, *39*, 056002. [[CrossRef](#)]
25. Croci, G.; Claps, G.; Cazzaniga, C.; Foggetta, L.; Muraro, A.; Valente, P. GEM-based detectors for thermal and fast neutrons. *Eur. Phys. J. Plus* **2015**, *130*, 1–8. [[CrossRef](#)]
26. Li, K.; Zhou, J.R.; Wang, X.D.; Xiong, T.; Zhang, Y.; Xie, Y.G.; Zhou, L.; Xu, H.; Yang, G.A.; Wang, Y.F.; et al. Study of a nTHGEM-based thermal neutron detector. *Chin. Phys. C* **2016**, *40*, 076002. [[CrossRef](#)]
27. Li, G.; Xie, Y.; Zhao, H.; Yan, W.-Q.; Li, Y.-L.; Peng, Z.-Y.; Hu, T.; Lv, J.-G.; Zhou, L. A new neutron detector based on ceramic THGEM and boron-coated meshes. *Radiat. Detect. Technol. Methods* **2018**, *2*, 1–9. [[CrossRef](#)]
28. Fang, Z.; Yang, Y.; Li, Y.; Wang, X. The research on the suppression of spurious neutrons for a neutron detector array that may be used in the neutron scattering. In Proceedings of the 2017 IEEE Nuclear Science Symposium and Medical Imaging Conference (NSS/MIC), Atlanta, GA, USA, 21–28 October 2017; pp. 1–4.
29. Agostinelli, S.; Allison, J.; Amako, K.; Apostolakis, J.; Araujo, H.; Arce, P.; Asai, M.; Axen, D.; Banerjee, S.; Barrand, G.; et al. GEANT4—a simulation toolkit. *Nucl. Instrum. Methods Phys. Res. Sect. A Accel. Spectrometers Detect. Assoc. Equip.* **2003**, *506*, 250–303. [[CrossRef](#)]
30. Allison, J.; Amako, K.; Apostolakis, J.E.A.; Araujo, H.; Dubois, P.A.; Asai, M.; Barrand, G.; Capra, R.; Chauvie, S.; Chytráček, R.; et al. Geant4 developments and applications. *IEEE Trans. Nucl. Sci.* **2006**, *53*, 270–278. [[CrossRef](#)]
31. Allison, J.; Amako, K.; Apostolakis, J.; Arce, P.; Asai, M.; Aso, T.; Bagli, E.; Bagulya, A.; Banerjee, S.; Barrand, G.; et al. Recent developments in Geant4. *Nucl. Instrum. Methods Phys. Res. Sect. A Accel. Spectrometers Detect. Assoc. Equip.* **2016**, *835*, 186–225. [[CrossRef](#)]
32. Azevedo, C.D.R.; Correia, P.M.M.; Carramate, L.; Silva, A.; Veloso, J. THGEM gain calculations using Garfield++: Solving discrepancies between simulation and experimental data. *J. Instrum.* **2016**, *11*, P08018. [[CrossRef](#)]
33. Pfeiffer, D.; De Keukeleere, L.; Azevedo, C.; Belloni, F.; Biagi, S.; Grichine, V.; Hayen, L.; Hanu, A.R.; Hřivnáčová, I.; Ivanchenko, V.; et al. Interfacing Geant4, Garfield++ and Degrad for the simulation of gaseous detectors. *Nucl. Instrum. Methods Phys. Res. Sect. A Accel. Spectrometers Detect. Assoc. Equip.* **2019**, *935*, 121–134. [[CrossRef](#)]
34. Deng, C.; Wang, Q.; Wu, Y.; Peng, S.; Liu, F.; Li, H.; Cheng, J.; Tuo, X. Preparation and characterization of boron films used for boron-lined gaseous neutron detectors. *J. Korean Phys. Soc.* **2021**, *79*, 606–612. [[CrossRef](#)]
35. Fang, Z.; Deng, C.; Guérard, B.; Yang, Y.; Li, Y.; Zhang, Z.; Wang, X. Realization and evaluation of the Boron Nano Particle-based drip-coating method for boron-lined gaseous neutron detectors. *J. Instrum.* **2019**, *14*, P12003. [[CrossRef](#)]
36. Charpak, G. Multiwire Chambers, Drift Chambers and Some of their Applications. *Europhys. News* **1979**, *10*, 7–10. [[CrossRef](#)]
37. Charpak, G.; Sauli, F. Multiwire proportional chambers and drift chambers. *Nucl. Instrum. Methods* **1979**, *162*, 405–428. [[CrossRef](#)]
38. Deng, C.; Liu, F.; Wang, Q.; Tuo, X.; Peng, S.; Wu, Y.; Yang, H.; Dai, H. Research on angle sensitivity of the boron-lined multilayer converter neutron detector. *Meas. Sci. Technol.* **2022**, *33*, 065901. [[CrossRef](#)]
39. Zhao, Y.; Cui, T.; Yang, Y. The design of a photoneutron source for the narcotic drugs detection in a large-truck. In Proceedings of the 2017 IEEE Nuclear Science Symposium and Medical Imaging Conference (NSS/MIC), Atlanta, GA, USA, 21–28 October 2017; pp. 1–3.
40. Cui, T.; Yang, Y.; Zhang, Z.; Zong, C.; Ming, S.; Wang, D. An e-LINAC driven PGNA system for concealed drug inspection. In Proceedings of the 2020 IEEE Nuclear Science Symposium and Medical Imaging Conference (NSS/MIC), Boston, MA, USA, 31 October–7 November 2020; pp. 1–2.

**Disclaimer/Publisher’s Note:** The statements, opinions and data contained in all publications are solely those of the individual author(s) and contributor(s) and not of MDPI and/or the editor(s). MDPI and/or the editor(s) disclaim responsibility for any injury to people or property resulting from any ideas, methods, instructions or products referred to in the content.